



ELSEVIER

Contents lists available at ScienceDirect

Materials Science & Engineering A

journal homepage: www.elsevier.com/locate/msea

Microstructure effect on hydrogen-induced cracking in TM210 maraging steel

Gang Wang^a, Yu Yan^a, Jinxu Li^{a,*}, Jingyu Huang^b, Lijie Qiao^a, Alex A. Volinsky^{a,c}

^a Corrosion and Protection Center, Key Laboratory for Environmental Fracture (MOE), University of Science and Technology Beijing, Beijing 100083, China

^b Beijing Xinfeng Machinery Factory, Beijing 100854, China

^c Department of Mechanical Engineering, University of South Florida, Tampa, FL, 33620, USA

ARTICLE INFO

Article history:

Received 22 June 2013

Received in revised form

22 July 2013

Accepted 25 July 2013

Available online 16 August 2013

Keywords:

Maraging steel

Hydrogen embrittlement

Reverted austenite

Martensite lath boundaries

ABSTRACT

Hydrogen embrittlement (HE) of TM210 maraging steel was studied by slow strain rate tensile and constant load tests. The over-aged sample exhibited the best resistance to HE, since HE susceptibility of the maraging steel does not depend on the strength, but rather on the reverted austenite content. The hydrogen concentration, observed by scanning Kelvin probe force microscopy, was enriched in the reverted austenite at the grain boundaries and martensite lath boundaries, resulting in hydrogen-induced cracks propagating along the grain boundaries and martensite lath boundaries.

© 2013 Elsevier B.V. All rights reserved.

1. Introduction

Maraging steels, development in the 1960s, have been widely used in aerospace industrial applications due to their ultra high strength and toughness, along with good formability. Solution-treated maraging steels have martensite with high dislocation density and a pronounced hardening effect, produced by Ni₃(Ti, Mo) or Fe₂Mo particles precipitation during the aging treatment [1–3]. When aged between 500 °C and 700 °C, the reverted austenite was also observed, and its content increased with the aging temperature, along with particles precipitation [3–4]. In addition, the presence of reverted austenite may considerably alter the strength and toughness of the alloy [5–7].

These steels are known to undergo severe hydrogen embrittlement (HE) when used in certain service environments [8–11]. Due to the ultra high strength, the maraging steels are more prone to suffer from hydrogen embrittlement. Numerous facts have shown that the HE severely threatens the safety of aerospace parts. Therefore, the HE problem in high strength steels has been addressed by researchers in recent years [12–19].

Hydrogen could be absorbed by the steel during environmental exposure, even in mild environments, such as water [16] or humid air [17–19]. Several researchers have shown that hydrogen diffuses to, and concentrates at the crack tips, where the hydrostatic stress is the maximum [20–22]. Studies have also demonstrated that the threshold stress, or the threshold stress intensity factor, decrease linearly with

the logarithm of hydrogen concentration [23–24]. When the applied stress is higher than the threshold stress for hydrogen-induced cracking (HIC), brittle cracks will initiate and propagate. In maraging steels, the precipitates not only act as the strengthening phase, but also as hydrogen traps. Since hydrogen solubility in the face-centered cubic (fcc) reverted austenite is much higher than in the body-centered tetragonal (bct) martensite, hydrogen concentration in the martensite will decrease, resulting in lower HE susceptibility, improved by the reverted austenite content. Hydrogen in martensite concentrates at grain and martensite lath boundaries, and, as a consequence, hydrogen-induced cracking initiates and propagates along the grain and martensite lath boundaries [11,25–26].

In this paper, the effect of the strength and the content of the reverted austenite on hydrogen induced cracking in maraging steel has been studied. Slow strain rate test (SSRT) and constant load tensile test were used to study the HE susceptibility of maraging steel, and the fracture morphology was examined to analyze the nucleation and propagation of hydrogen assisted cracks. The scanning Kelvin probe force microscopy (SKPFM) was also employed to show the influence of hydrogen on the brittle crack growth behavior.

2. Experimental procedure

2.1. Materials

The material examined in this study is TM210 maraging steel. The chemical composition of the steel in weight percent is 18% Ni, 10% Co, 4.5% Mo, 1.1% Ti, 0.1% Al, and the balance is Fe. The steel was solution treated at 820 °C for 1 h, air cooled and then aged at 465 °C,

* Corresponding author. Tel.: +86 10 62334493; fax: +86 10 62332345.
E-mail address: jxli65@ustb.edu.cn (J. Li).

490 °C, 510 °C for 3 h, respectively. Correspondingly, the three heat treatment conditions could be named as under-aged, peak-aged and over-aged. In addition, samples aged at 580 °C and 640 °C were also prepared.

For slow strain rate tests (SSRT) and constant load tensile tests, cylindrical specimens with a gauge length of 40 mm and 4 mm diameter were employed. For magnetic force microscopy (MFM) measurements, samples with the dimensions of $10 \times 10 \text{ mm}^2$ were used. For SKPFM analysis, the electrochemical pre-charged wedge-open loading (WOL) sample was employed to investigate the influence of hydrogen on the brittle crack growth behavior. The outer surface of the sample was wet ground with SiC papers up to 2000 grit, mechanical polished using a diamond paste to $1.5 \mu\text{m}$, and then cleaned with ethanol.

2.2. Slow strain rate test

HE susceptibility of the steel was assessed by performing slow strain rate tests. First, tests were carried out in air to provide a baseline for comparison. At a strain rate of $1 \times 10^{-7} \text{ s}^{-1}$, SSRT was performed in the solution with dynamic hydrogen charging. The relative plasticity loss is chosen as HE susceptibility I , i.e., $I(\psi) = (\psi_a - \psi_H) / \psi_a \times 100\%$ or $I(\delta) = (\delta_a - \delta_H) / \delta_a \times 100\%$, where ψ_a and ψ_H or δ_a and δ_H is reduction of area, or elongation in air and with dynamic hydrogen charging conditions, respectively. Sometimes, the relative strength loss is also chosen as HE susceptibility, i.e., $I(\text{UTS}) = (\text{UTS}_a - \text{UTS}_H) / \text{UTS}_a \times 100\%$, where UTS_a and UTS_H is the ultimate tensile strength in air and during charging, respectively. The sample was electrolytically charged at a current density of 0.5 mA/cm^2 in 0.2 mol/L NaOH electrolyte with an addition of $0.22 \text{ g/L thiourea (H}_2\text{NCSNH}_2\text{)}$.

2.3. Constant load tensile test

Constant load tensile tests were performed to evaluate the service life and the threshold stress of the steel in different environments. The lever ratio of the constant load tensile testing machine is 1:50. Four kinds of charging conditions were used for the over-aged samples. The fracture time was recorded at each applied load, and the test time was set at 720 h. The threshold stress was calculated by the mean value of the minimum stress that lead to fracture, and the maximum stress that causes no fracture during the test time. Moreover, the difference between the two stresses should be less than or equal to 20% of the threshold stress in order to ensure that the measuring error of the threshold stress is less than 10% [27]. The hydrogen concentration in the sample that did not fracture was measured by the G4 PHOENIX DH hydrogen analyzer. A ZEISS SURPA55 scanning electron microscope (SEM) was used to examine the fracture surfaces after the SSRT and constant load tensile tests.

2.4. Crack propagation

In order to identify the crack propagation path, a modified WOL specimen was employed. The specimen was fatigued to generate a pre-crack, and the surface with fatigue crack was mechanically polished to mirror finish. The fatigued WOL sample was electrochemically hydrogen charged after etching by aqua regia, and loaded with a screw. The microscopic morphology in the vicinity of the crack tip was observed with the optical microscope.

SKPFM was used to study the surface potential distribution near hydrogen-induced crack tip. Scanning Kelvin probe force microscopy, which is based on high-resolution atomic force microscopy (AFM) and standard Kelvin probe technology [28–29], allows obtaining not only topographic images, but also surface potential images in the same area simultaneously. The morphology and surface potential were measured using a Dimension AFM (Nanoscope V, Veeco Instruments Inc.). The equipment was operated in a room with a constant temperature of

25 °C and 25% relative humidity. The surface potential was measured by SKPFM in a tapping/lift mode with a lift height of 60 nm. All experiments were performed at room temperature.

3. Results

3.1. Microstructure

Three kinds of specimens, i.e., under-aged, peak-aged and over-aged have similar metallographic microstructure, as shown in Fig. 1(a), where martensite, the phase interfaces and grain boundaries can be distinguished. The difference between them is the type and amount of precipitation, as well as the reverted austenite content. However, the reverted austenite and precipitates cannot be identified by optical microscopy. Since martensite is a ferromagnetic phase, and austenite is a paramagnetic phase, the two phases could be distinguished by their magnetic properties using Magnetic Force Microscopy (MFM).

The MFM images of various aging conditions are shown in Fig. 1(b–f). As seen in Fig. 1(b–f), the contrast of the MFM images reflects the strength of the magnetic field. At under-aged conditions of 465 °C, striped magnetic domains are obvious, as seen in Fig. 1(b). With increasing aging temperature from 490 °C to 640 °C, the striped magnetic domains become weaker, as seen in Fig. 1(c–f). It is the appearance of the paramagnetic austenite that enables the decrease of the magnetic field. Fig. 1(b–f) shows that the amount of reverted austenite increases with the aging temperature in the 465 °C to 640 °C range.

3.2. HE susceptibility and threshold stress of hydrogen-induced cracking

3.2.1. HE susceptibility

Fig. 2(a) shows the stress–strain curves for samples of three aging states in air and SSRT during dynamic charging. The mechanical properties of the samples with different aging conditions are almost the same in air. However, for SSRT during charging, the specimen failed in the elastic regime, and all of the mechanical properties have been dramatically reduced. HE susceptibility was calculated, as listed in Table 1. The variation of HE susceptibility with the yield strength is plotted in Fig. 2(b). The HE susceptibility does not increase with the strength. The relative elongation loss, $I(\delta)$, has the same value for the three aging conditions. However, the relative reduction in area, $I(\psi)$, and the relative strength loss, $I(\text{UTS})$, indicate that the over-aged sample exhibits the best resistance to HE, and the under-aged sample is worst.

3.2.2. Threshold stress of hydrogen-induced cracking

Time to failure of HIC during dynamic charging with a current density of 0.5 mA/cm^2 vs. normalized stress, σ/UTS , is shown in Fig. 3(a). For the same normalized stress, the time to failure of the under-aged sample is the shortest, followed by the peak-aged sample, and the over-aged sample the longest, e.g., when $\sigma/\text{UTS} = 0.35$, the failure time is 5.2 h, 55.1 h and 159.2 h, respectively. This means that the over-aged sample has the best resistance to HIC.

For the over-aged sample, time to failure of HIC in various charging conditions vs. normalized stress is plotted in Fig. 3(b). Based on the data in Fig. 3(b), the relationship between the failure time, t_F , and the normalized stress, σ/UTS , can be expressed as:

$$\sigma/\text{UTS} = 0.53 \exp(-t_F/182.68) + 0.44 \quad (\text{in water}) \quad (1)$$

$$\sigma/\text{UTS} = 0.55 \exp(-t_F/58.74) + 0.45 \quad (0.1 \text{ mA/cm}^2 \text{ charged}) \quad (2)$$

$$\sigma/\text{UTS} = 0.73 \exp(-t_F/59.37) + 0.275 \quad (0.5 \text{ mA/cm}^2 \text{ charged}) \quad (3)$$

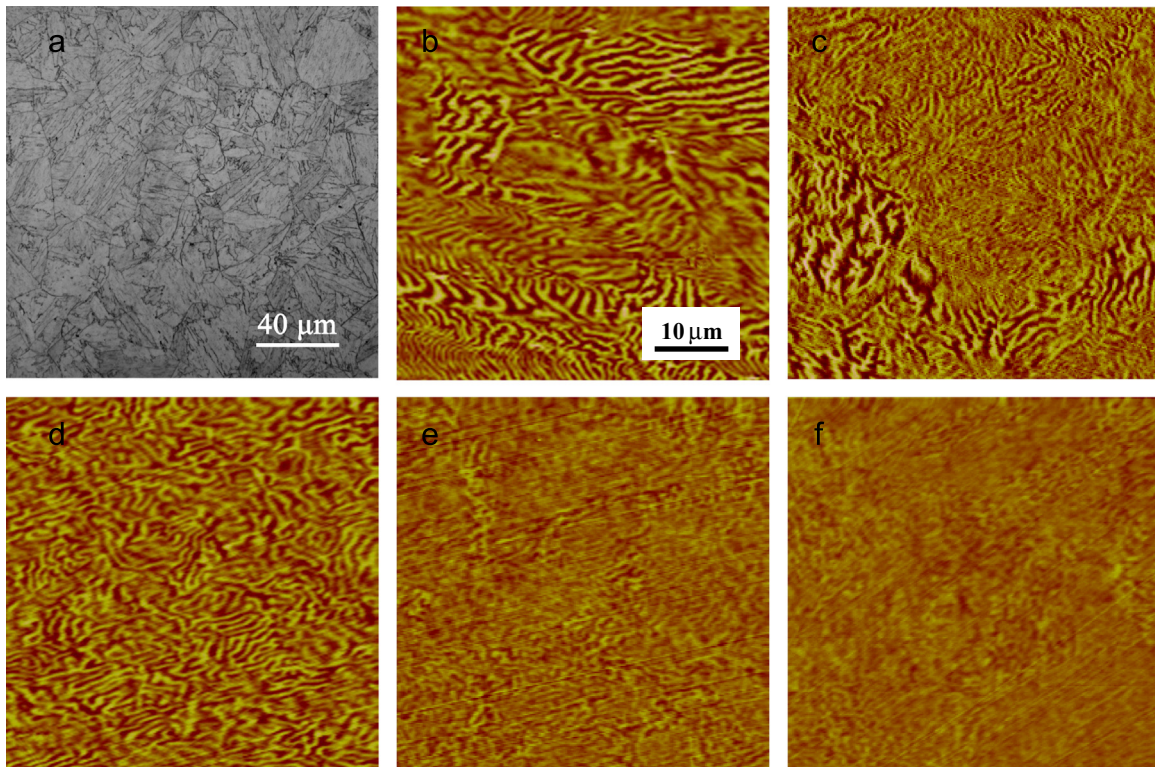


Fig. 1. (a) Metallographic image of the TM210 maraging steel; MFM images of the maraging steel at different aging temperatures: (b) 465 °C; (c) 490 °C; (d) 510 °C; (e) 580 °C; and (f) 640 °C. Micron bars are the same for (b–f).

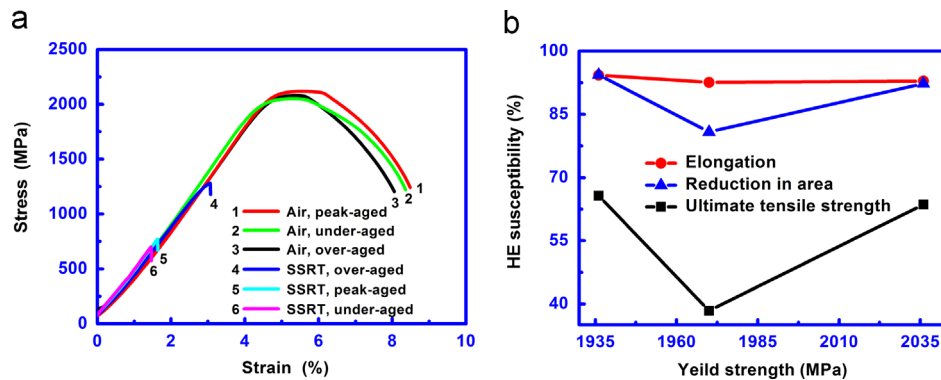


Fig. 2. (a) Stress–strain curves of the samples aged at different conditions in air and during dynamic charging and (b) HE susceptibility vs. yield strength.

Table 1

Tensile properties of TM210 specimens aged at different conditions, tested in air or hydrogen charged at room temperature.

	Properties	YS (MPa)	UTS (MPa)	δ (%)	ψ (%)	$l(\text{UTS})$ (%)	$l(\delta)$ (%)	$l(\psi)$ (%)
In air	Under-aged	1936	2041	5.3	53.7	–	–	–
	Peak-aged	1970	2118	5.6	53.0	–	–	–
	Over-aged	2036	2079	5.4	51.1	–	–	–
During charging	Under-aged	–	700	0.3	3.0	65.7	94.3	94.4
	Peak-aged	–	771	0.4	4.1	63.6	92.9	92.3
	Over-aged	–	1281	0.4	9.8	38.4	92.6	80.8

$$\sigma/\text{UTS} = 0.78\exp(-t_F/31.92) + 0.225 \quad (10 \text{ mA/cm}^2 \text{ charged}) \quad (4)$$

Based on Fig. 3(b), the normalized threshold stress of HIC, $\sigma_{\text{th}}/\text{UTS}$, can be also calculated, as listed in Table 2. The hydrogen concentration of the samples that did not fracture in 720 h are also listed in Table 2. The normalized threshold stress of HIC decreases with hydrogen concentration, as shown in Fig. 4.

3.3. Fracture modes of SSRT and constant load tensile test

Fracture surfaces were studied using SEM after tensile tests. Fig. 5(a–c) are low magnification views of aged maraging steel specimens after tensile test in air. Regardless of the aging conditions, specimens exhibited nearly the same necking flat fracture, with a typical ductile fractography surrounded by the shear lip.

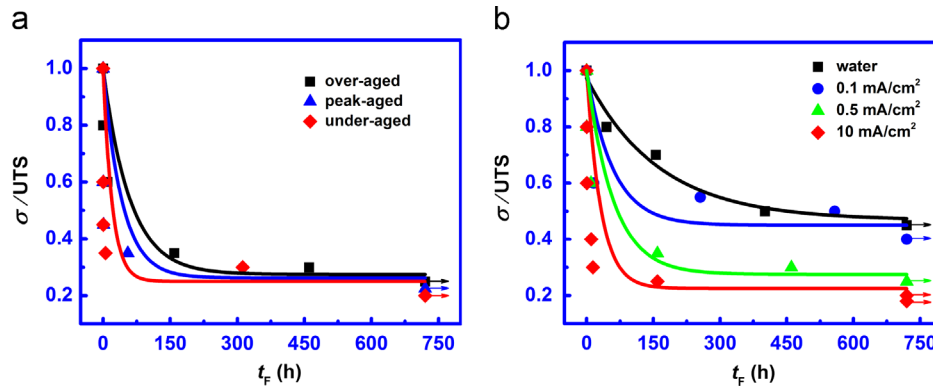


Fig. 3. (a) Normalized stress, σ/UTS , vs. time to failure of specimens aged in three different conditions during dynamic charging with 0.5 mA/cm^2 current density. (b) Normalized stress, σ/UTS , vs. time to failure of the over-aged charged specimens.

Table 2

Normalized threshold stress of HIC and hydrogen concentration in over-aged samples charged at different conditions.

Charging condition	Water	0.1 mA/cm ²	0.5 mA/cm ²	10 mA/cm ²
σ_{th}/UTS	0.475	0.45	0.275	0.225
C_H (ppm)	1.09	9.43	11.83	14.00

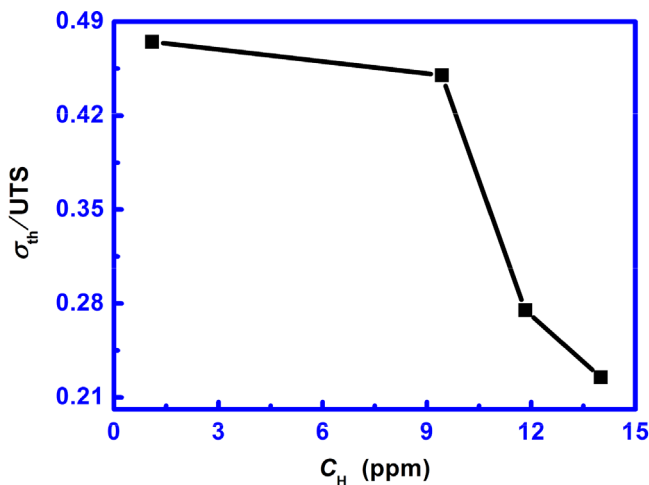


Fig. 4. Normalized threshold stress of HIC, σ_{th}/UTS vs. hydrogen concentration, C_H .

The tensile fracture surfaces for dynamically charged specimens are shown in Fig. 5(d–f). A small fraction of ductile region surrounded by brittle fracture regions with secondary cracks on the fracture surface was found for the under-aged specimen (Fig. 5(d)) and the peak-aged specimen (Fig. 5(e)). For the over-aged specimen, half shear lip could also be seen (Fig. 5(f)).

In Fig. 5(d), there are three regions, i.e., intergranular initiation region (IG), quasi-cleavage propagation region (QC) and ductile fracture region (D). Magnified IG and QC regions are shown in Fig. 6(a) and (b), respectively. During SSRT, HIC initiate along grain boundaries from the surface of the specimen, as shown in Fig. 6(a). HIC propagates along martensite lath boundaries, resulting in quasi-cleavage fracture, as seen in Fig. 6(b). At the beginning of the SSRT, the applied stress was too low to generate voids or cracks, and hydrogen had enough time to diffuse into the sample. The diffusion distance is calculated as

$$x = \alpha\sqrt{Dt} \quad (5)$$

where x is the diffusion distance, α is a constant, t is the hydrogen diffusion time, and D is the hydrogen diffusion coefficient,

obtained from the electrochemical hydrogen permeation test. For the under-aged samples, D is $4.2 \times 10^{-9} \text{ cm}^2/\text{s}$, and the time from the beginning of SSRT to fracture is 40.6 h, so the corresponding diffusion distance is about 0.99 mm. It is consistent with the width of initiation and propagation regions (i.e., IG + QC) in Fig. 5(d). The dimple region in the center of the fracture surface indicates that it failed in a ductile manner, and hydrogen did not diffuse to this region before the final failure occurred.

For a constant load sample with $\sigma/UTS = 0.5$ in water, the failure time was 401.2 h. There are a lot of secondary cracks, perpendicular to the loading direction at the surface of the fractured specimen, as seen in Fig. 7(a). The fracture surface is shown in Fig. 7(b). The center region of the sample is quasi-cleavage because hydrogen diffused to reach the center of the sample after 401.2 h.

4. Discussion

4.1. Strength and reverted austenite effects on HE susceptibility

Generally, the hydrogen embrittlement (HE) susceptibility increases with the strength of the steel. However, for TM210 maraging steel, HE susceptibility does not change monotonously with the strength. The results in this paper show that the over-aged sample with medium strength exhibited the best resistance to HE.

Previous researches of maraging steels confirmed that the martensite will transform into reverted austenite during the aging treatment, and the fcc reverted austenite has much higher hydrogen solubility than the bct martensite, so the HE susceptibility of austenite is lower than that of the martensite, thus HIC preferentially occurs in martensite [9,30–33]. Higher reverted austenite content corresponds with the lower hydrogen concentration in martensite, which lowers HE susceptibility of the sample. The MFM images in Fig. 1(b–f) suggest that the amount of reverted austenite increased with the aging temperature in the 465–640 °C range. Comparing the peak-aged and the under-aged samples, the higher strength increases HE susceptibility, but higher content of the reverted austenite decreases the HE susceptibility, resulting in basically the same HE susceptibility of the peak-aged and under-aged samples, as shown in Fig. 2(b). The strength of the over-aged samples is lower and the content of reverted austenite is higher than the peak-aged samples, resulting in the lowest HE susceptibility.

4.2. Hydrogen and stress effects on hydrogen-induced cracking

During charging under constant load, the hydrogen concentration at grain boundaries on the surface of the sample has the

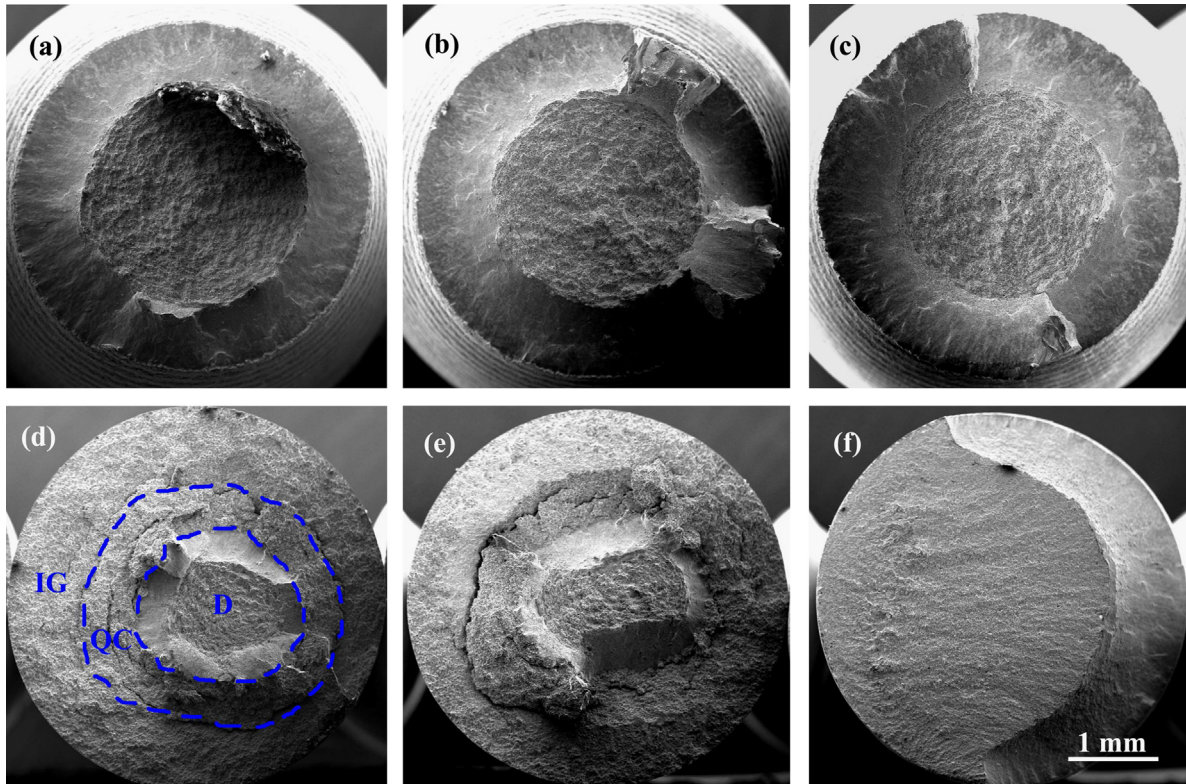


Fig. 5. Low magnification view of the specimen fracture surface: (a) under-aged; (b) peak-aged; (c) over-aged, tested in air and (d) under-aged; (e) peak-aged; (f) over-aged, tested with dynamic hydrogen charged at a strain rate of $1 \times 10^{-7} \text{ s}^{-1}$.

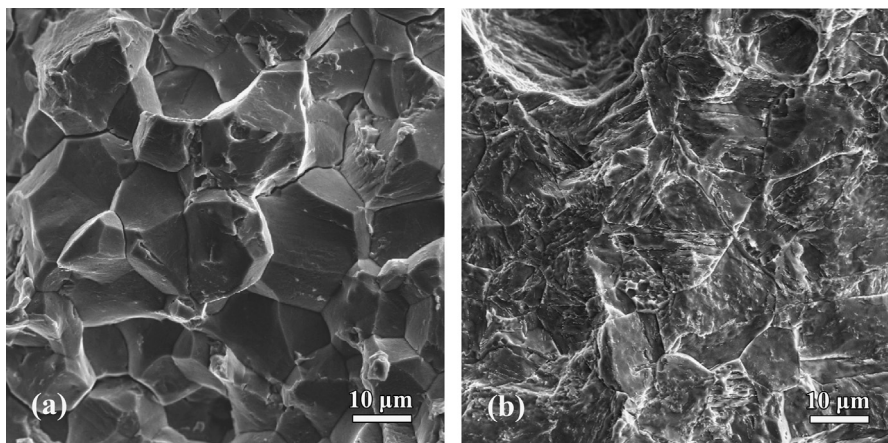


Fig. 6. (a) Magnified region of IG and (b) QC regions in Fig. 5(d).

maximum, which increases with time by stress-induced diffusion. When the hydrogen concentration at grain boundaries reaches a critical value, the cohesive strength at grain boundaries decreases, resulting in initiating of HIC along grain boundaries on the surface under constant load. When the applied constant stress is less than the intergranular cohesive strength, decreased by enriched hydrogen, no HIC occurs. Therefore, there exists a threshold stress below which no HIC occurs for constant charging conditions. Higher hydrogen concentration lowers cohesive strength at grain boundaries, therefore, lower constant load will induce HIC initiation. That is to say that the threshold stress of HIC decreases with hydrogen concentration, C_H , as shown in Fig. 4. For the same charging conditions, higher constant load results in lower HIC critical hydrogen concentration, which shortens the hydrogen enrichment time, as shown in Fig. 3(b). As soon as HIC initiates, there is a stress concentration ahead of the crack, which increases

with crack propagation. Load stress concentration induces crack propagation along the region of lower hydrogen enrichment, e.g., the martensite lath, resulting in quasi-cleavage fracture. When the stress concentration is high enough, existing hydrostatic stress ahead of the crack tip will induce initiation and connection of voids, resulting in dimple fracture.

4.3. Microstructure and HIC propagation path

After HIC initiates and propagates along the grain boundaries, HIC will propagate along the grain and/or martensite lath boundaries, as seen in Fig. 8(a), with the corresponding fractograph shown in Fig. 8(b).

The initiation and propagation of HIC are closely associated with the distribution of hydrogen in steel. By means of SKPFM and metallography, the hydrogen-induced variation of the surface

potential has been examined. Fig. 9(a) is the surface potential image in the vicinity of the crack tip, where brighter areas around the crack indicate higher hydrogen concentration. For clarity, the corresponding

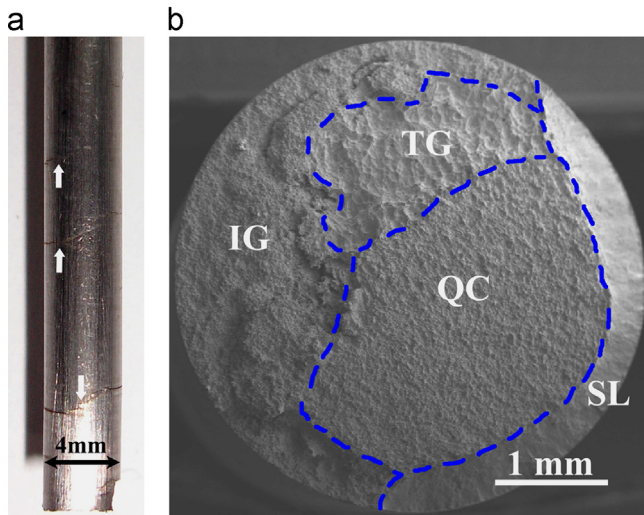


Fig. 7. (a) Secondary cracks at the surface and (b) fracture surface of constant load sample with $\sigma/UTS=0.5$ in water.

microscopic morphology was examined by optical microscopy, with the corresponding potential maxima from Fig. 9(a) highlighted by the yellow points in Fig. 9(b). One can see that most of the yellow points are located at the martensite lath boundaries, or grain boundaries, that is, hydrogen prefers to concentrate at the martensite lath or grain boundaries, where the reverted austenite is prone to nucleating. The enrichment of hydrogen in these regions decreases the cohesive strength between the boundaries, so the hydrogen-induced cracks are more inclined to propagate along the martensite lath or grain boundaries.

5. Conclusions

In this paper, hydrogen embrittlement was studied by slow strain rate tensile and constant load tests. With the aid of SEM and SKPFM, the hydrogen-induced cracking behavior was identified. The following conclusions can be made:

- (1) For the TM210 maraging steel, the over-aged sample exhibits the best resistance to HE, and the HE susceptibility depends not only on the strength, but also on the reverted austenite content.
- (2) The hydrogen-induced cracking initiates from the surface of the sample, and propagates along the hydrogen-enriched grain boundaries or martensite lath boundaries.

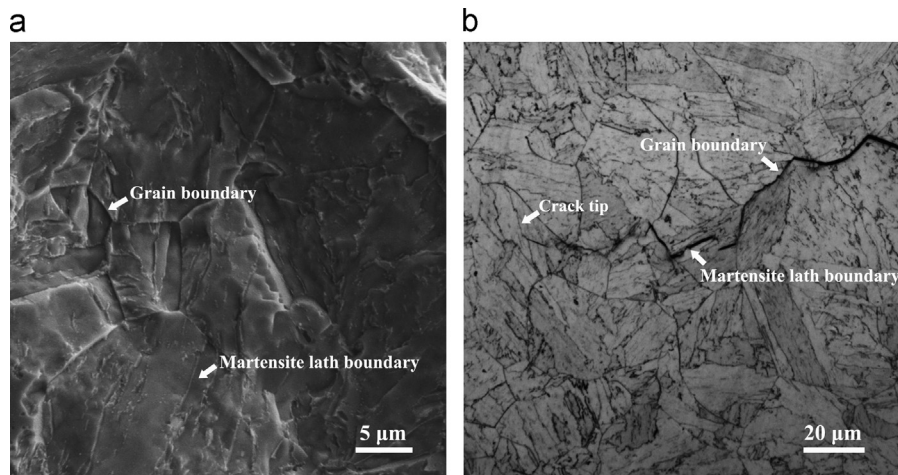


Fig. 8. HIC propagating along grain boundaries and/or martensite lath boundaries: (a) optical micrograph and (b) SEM fractograph.

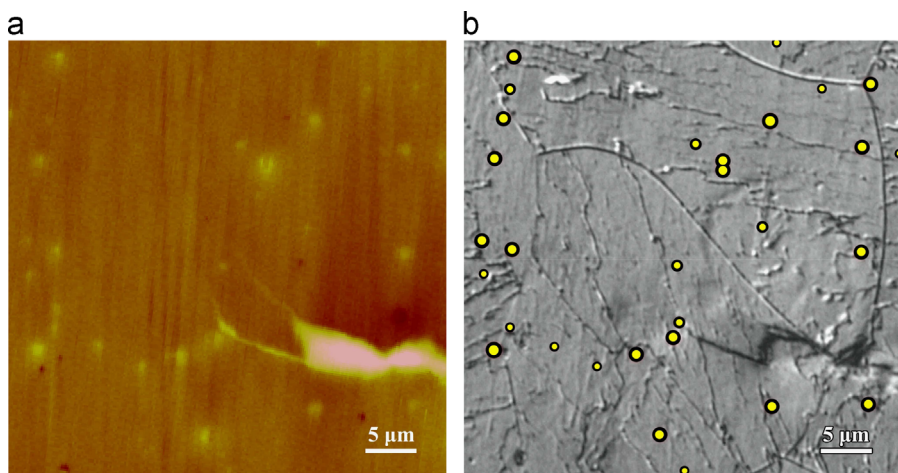


Fig. 9. (a) The surface potential image and (b) the corresponding optical micrograph in the vicinity of the crack tip. The yellow points in (b) correspond to the high potential points in (a) (For interpretation of the references to color in this figure legend, the reader is referred to the web version of this article.).

Acknowledgments

The authors acknowledge support from the National Natural Science Foundation of China (No. 51071025) and 973 program (No. 2014CB643301).

References

- [1] V.K. Vasudevan, S.J. Kim, C.M. Wayman, *Metall. Trans. A* 21A (1990) 2655–2668.
- [2] U.K. Viswanathan, G.K. Dey, M.K. Asundi, *Metall. Mater. Trans. A* 24 (1993) 2429–2442.
- [3] R. Tewari, S. Mazumder, I.S. Batra, G.K. Dey, S. Banerjee, *Acta Mater.* 48 (2000) 1187–1200.
- [4] J. Hutchings, G. Sanderson, *Corros. Sci.* 16 (1976) 545–549.
- [5] A. Markfeld, A. Rosen, *Mater. Sci. Eng.* 46 (1980) 151–157.
- [6] U.K. Viswanathan, G.K. Dey, V. Sethumadhavan, *Mater. Sci. Eng. A* 398 (2005) 367–372.
- [7] R. Schnitzer, G.A. Zickler, E. Lach, H. Clemens, S. Zinner, T. Lippmann, H. Leitner, *Mater. Sci. Eng. A* 527 (2010) 2065–2070.
- [8] B.G. Pound, *Corros. Sci.* 42 (2000) 1941–1956.
- [9] L.W. Tsay, Y.F. Hu, C. Chen, *Corros. Sci.* 47 (2005) 965–976.
- [10] L.W. Tsay, M.Y. Chi, Y.F. Wu, J.K. Wu, D.Y. Lin, *Corros. Sci.* 48 (2006) 1926–1938.
- [11] P.S. Pao, R.P. Wei, *Scripta Metall.* 11 (1977) 515–520.
- [12] R. Nishimura, D. Shiraishi, Y. Maeda, *Corros. Sci.* 46 (2004) 225–243.
- [13] S. Ramamurthy, W.M.L. Lau, A. Atrens, *Corros. Sci.* 53 (2011) 2419–2429.
- [14] X.S. Du, Y.J. Su, J.X. Li, L.J. Qiao, W.Y. Chu, *Corros. Sci.* 65 (2012) 278–287.
- [15] D. Hardie, E.A. Charles, A.H. Lopez, *Corros. Sci.* 48 (2006) 4378–4385.
- [16] W.Y. Chu, T.H. Liu, C.M. Hsiao, S.Q. Li, *Corrosion* 37 (1981) 320–327.
- [17] Y.P. Zhang, D.M. Shi, W.Y. Chu, L.J. Qiao, Y.L. Shi, S.L. Zheng, S.B. Wang, *Mater. Sci. Eng. A* 471 (2007) 34–37.
- [18] E. Akiyama, K. Matsukado, M.Q. Wang, K. Tsuzaki, *Corros. Sci.* 52 (2010) 2758–2765.
- [19] E. Akiyama, S.J. Li, T. Shinohara, Z.G. Zhang, K. Tsuzaki, *Electrochim. Acta* 56 (2011) 1799–1805.
- [20] L.J. Qiao, J.L. Luo, X. Mao, *Corrosion* 54 (1998) 115–120.
- [21] H.B. Xue, Y.F. Cheng, *Electrochim. Acta* 55 (2010) 5670–5676.
- [22] A.T. Yokobori Jr., Y. Chinda, T. Nemoto, K. Satoh, T. Yamada, *Corros. Sci.* 44 (2002) 407–424.
- [23] W.Y. Chu, L.J. Qiao, Y.B. Wang, Y.H. Cheng, *Corrosion* 55 (1999) 667–673.
- [24] G.H. Yu, Y.H. Cheng, L. Chen, L.J. Qiao, Y.B. Wang, W.Y. Chu, *Corrosion* 53 (1997) 762–769.
- [25] R.P. Wei, G.W. Simmons, *Scr. Metall.* 10 (1976) 153–157.
- [26] L.W. Tsay, H.L. Lu, C. Chen, *Corros. Sci.* 50 (2008) 2506–2511.
- [27] W.Y. Chu, L.J. Qiao, Q.Z. Chen, K.W. Gao, *Fracture and Environmental Fracture*, Science Press, Beijing, 2000.
- [28] M. Jonsson, D. Thierry, N. LeBozec, *Corros. Sci.* 48 (2006) 1193–1208.
- [29] M. Li, L.Q. Guo, L.J. Qiao, Y. Bai, *Corros. Sci.* 60 (2012) 76–81.
- [30] D. Figueroa, M.J. Robinson, *Corros. Sci.* 52 (2010) 1593–1602.
- [31] G.M. Pressouyre, I.M. Bernstein, *Acta Metall.* 27 (1979) 89–100.
- [32] R.O. Ritchie, M.O. Castro Cedeno, V.F. Zackay, E.R. Parker, *Metall. Trans. A* 9A (1978) 35–40.
- [33] D. Figueroa, M.J. Robinson, *Corros. Sci.* 50 (2008) 1066–1079.